1

Basic Science of PET and PET/CT

David W. Townsend

Introduction

Historical Background

The past few years have seen the transition of positron emission tomography (PET) from the research domain into mainstream clinical applications for oncology (1). The emergence of PET as the functional imaging modality of choice for diagnosis, staging, therapy monitoring, and assessment of recurrence in cancer has led to increasing demand for this advanced imaging technology. The recognition that functional imaging modalities such as PET may provide an earlier diagnosis and more accurate staging than conventional anatomic imaging has promoted the technology, particularly as PET is now a reimbursed imaging procedure in the United States for many types of cancer. Although PET offers an extensive array of different radiopharmaceuticals, or molecular probes, to image different aspects of physiology and tumor biology, currently the most widely used PET tracer is the fluorinated analogue of glucose, ^{18}F-2-deoxy-D-glucose (FDG). The increased uptake of glucose in malignant cells has been well known for many years (2), and although FDG is not a specific probe for cancer, nonspecificity can be a useful property when identifying and staging disease by a survey of the whole body. The widespread use of FDG is facilitated by the half-life of ^{18}F (110 min), which is convenient for transportation from a remote cyclotron and compatible with typical whole-body PET imaging times of 20 min or more following a 60- to 90-min uptake period.

The recent development of combined PET/CT instrumentation is an important evolution in imaging technology. Since the introduction of the first prototype computed tomography (CT) scanner in the early 1970s, tomographic imaging has made significant contributions to the diagnosis and staging of disease. Rapid commercial development followed the introduction of the first CT scanner in 1972, and within 3 years of its appearance more than 12 companies were marketing, or intending to market, CT scanners; about half that number actually market CT scanners today. With the introduction of magnetic resonance imaging (MRI) in the early 1980s, CT was, at that time, predicted to last another 5 years at most before being replaced by MRI for anatomic imaging. Obviously this did not happen, and today, with multislice detectors, spiral acquisition, and subsecond rotation times, CT continues to develop and play a major role in clinical imaging, especially for anatomic regions outside the brain.

Functional imaging, as a complement to anatomic imaging, has been the domain of nuclear medicine ever since the early 1950s. Initially, planar imaging with the scintillation (gamma) camera invented by Anger in 1958 was the mainstay of nuclear medicine. Even today, the widely used scintillation camera still follows Anger's original design, comprising a large sodium iodide crystal and collimator, with photomultiplier tubes as the photodetectors. In modern nuclear medicine, planar scintigraphy has been extended to tomography by the development of Single Photon Emission Computed Tomography (SPECT), which can be helpful for certain clinical applications. Although early SPECT systems actually predated CT, the real growth in SPECT did not occur until after the appearance of CT when similar reconstruction algorithms to those used in CT were applied to the reconstruction of parallel projections from SPECT data acquired by a rotating gamma camera.

Functional imaging with positron-emitting isotopes was first proposed in the early 1950s as an imaging technique that could offer greater sensitivity than conventional nuclear medicine techniques with single photon-emitting isotopes. The SPECT collimator is eliminated and replaced by electronic collimation—the coincident detection of two photons from positron annihilation—greatly increasing the sensitivity of the imaging system. However, other than some early prototypes in the 1960s, instrumentation to image positron emitters did not emerge seriously until the 1970s, and the first commercial PET scanners date from around 1980, about the time MRI also became commercially available.

PET was initially perceived as a complex and expensive technology requiring both a cyclotron to produce the short-lived PET radioisotopes and a PET scanner to image the tracer distribution in the patient. Consequently, during the 1970s, PET did not experience the explosive growth of CT, nor, during the 1980s, the comparable growth of MRI. In fact, it was not until the 1990s that PET became recognized as an important technique for imaging cancer by mapping glucose utilization throughout the body with FDG. The elevated utilization of glucose by malignant cells (2) allows cancerous tissue to be identified anywhere in the body, even though it may have no anatomic correlate that would allow identification on a CT scan. The effectiveness of FDG-PET imaging for diagnosing and staging malignant disease was officially recognized when the Centers for Medicare and Medicaid Services (CMS) approved reimbursement for a number of cancers in 1998. Following that decision, the application of FDG-PET for imaging cancer expanded rapidly, although still not at a rate that has ever fully rivaled the growth of the dominant anatomic imaging modalities CT and MRI during the 1970s and 1980s, respectively.

Combining Anatomy and Function

The corporate environments that developed these different imaging technologies, the medical specialties of radiology and nuclear medicine that were responsible for acquiring and operating them, and the differing chronology of clinical acceptance described here each contributed to ensuring CT and PET followed separate and distinct developmental paths. Both modalities have their strengths. CT scanners image anatomy with high spatial resolution, although malignant disease can generally only be identified from the presence of abnormal masses or from size changes in lymph nodes. PET, on the other hand can identify a functional abnormality in, for example, a normal-sized lymph node, although accurate localization of the node may be difficult, or even impossible, from the PET scan alone. To initiate the evolution in imaging technology that was required to physically integrate CT and PET (3) in a single device, initial skepticism from both the corporate environment and the medical profession had to be overcome. The key was to design and develop a research prototype PET/CT scanner within the context of National Institutes of Health (NIH) grant-funded collaboration between academia and industry. The first combined PET/CT prototype scanner was completed in 1998 (4), and clinical evaluation began in June of that year. The initial studies with the prototype (5–8) demonstrated a number of significant advantages of PET/CT: that functional abnormalities could now be accurately localized, that normal benign uptake of a nonspecific tracer such as FDG could be distinguished from uptake resulting from disease, and that confidence in reading both the PET and the CT increases significantly by having the anatomic and functional images routinely available and accurately aligned for every patient.

Although it may seem that, in many cases, it would be equally effective to view separately acquired CT and PET images for a given patient on adjacent computer displays, with (9) or without software registration, experience in the past 4 years with commercial PET/CT scanners has highlighted numerous unique advantages of the new technology. A number of these advantages were anticipated in the original PET/CT proposal, but others were unexpected and have only emerged since the technology became more widely available for clinical imaging.

The purpose of this chapter is to present the physical basis of PET and review aspects of the instrumentation that have been developed to image positron-emitting distributions. The design objectives of emerging PET/CT technology are described, and the status of current instrumentation and CT-based attenuation correction methodology are reviewed. Operation of PET/CT technology within the clinical setting opens up new possibilities for disease diagnosis, staging, and monitoring response to therapy. Although specific clinical applications are discussed in depth elsewhere in this volume, some general protocol definitions and refinements are presented here.

Physical Principles of PET Imaging

The principles of imaging tissue function in vivo with PET are summarized in Figure 1.1. Multiple steps are involved in the PET process, beginning with the selection and production of a suitable molecular probe, a pharmaceutical labeled with a positron-emitting radionuclide, the administration of the probe to the patient, and finally the imaging of the distribution of the probe in the patient. Positron emitters are neutron-deficient isotopes that achieve stability through the nuclear transmutation of a proton into a neutron. As shown in Figure 1.1a, this process involves the emission of a positive electron, or positron (β^+) and an electron neutrino (ν_e). The energy spectrum of the emitted positron depends on the specific isotope, with typical endpoint energies varying from 0.6 MeV for ^{18}F up to 3.4 MeV for ^{82}Rb. After emission, the positron loses energy by interactions in the surrounding tissue until it annihilates with an electron, as shown schematically in Figure 1.1b. The range that the positron travels in tissue obviously depends on the energy with which it is emitted, and the (electron) density of the surrounding tissue. The two annihilation photons are emitted in approximately opposite directions and are detected in coincidence; in this example, a coincidence is defined by two photons that are registered within a time interval of 2τ ns, where τ is the electronic coincidence time window.

Positron emitters such as ^{18}F are used to label substrates such as deoxyglucose (DG) (Figure 1.1c) to create

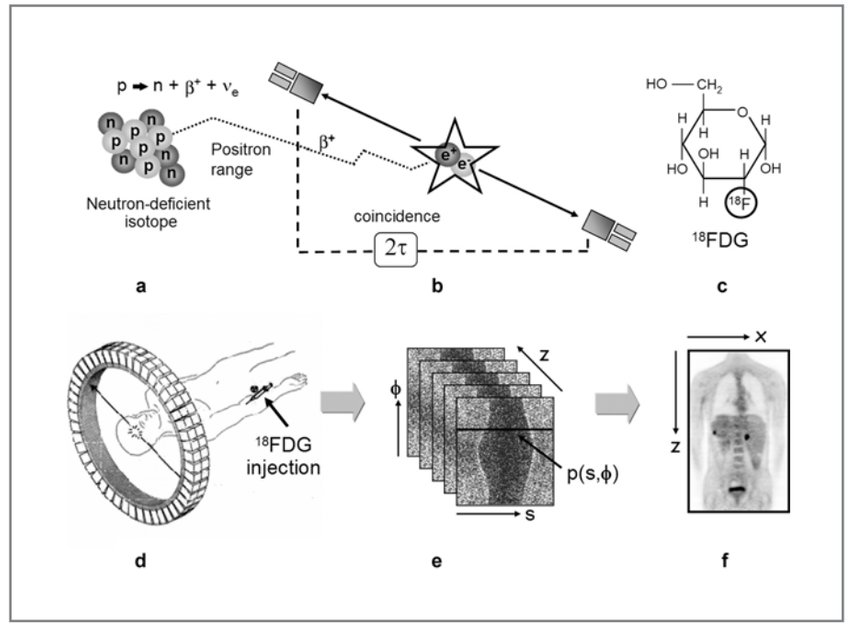

Figure 1.1. The principles of PET imaging shown schematically: (**a**) the decay of a neutron-deficient, positron-emitting isotope; (**b**) the detection in coincidence of the annihilation photons within a time window of 2τ ns; (**c**) the glucose analogue deoxyglucose labeled with the positron emitter ^{18}F to form the radiopharmaceutical FDG; (**d**) the injection of the labeled pharmaceutical and the detection of a pair of annihilation photons in coincidence by a multiring PET camera; (**e**) the collection of the positron annihilation events into sinograms wherein each element of the sinogram contains the number of annihilations in a specific projection direction; and (**f**) a coronal section of the final, reconstructed whole-body image mapping the utilization of glucose throughout the patient.

the radiopharmaceutical FDG. The radioactive tag is then transported by the circulation and incorporated into the organ of interest through metabolism of the pharmaceutical. For FDG, the relevant metabolic process is glucose utilization. The radiopharmaceutical is first injected into the patient, and the patient is then positioned in the PET scanner, a circular configuration of detectors (Figure 1.1d). The gamma ray pairs from positron annihilation are captured in coincidence by opposing detectors. The pairs of coincident photons (events) that are detected are stored in matrices (sinograms) where each row in the matrix represents a parallel projection, $p(s, \phi)$, of the activity distribution in the patient at a specific angle (ϕ) and axial position (z) (Figure 1.1e); s is the radial coordinate within a given parallel projection. An image reconstruction algorithm is applied to the sinogram data to recover the underlying radioactivity distribution, thus indirectly mapping the functional process that created the distribution of the positron emitter. For the radiopharmaceutical FDG, the images shown in Figure 1.1f are maps of FDG accumulation throughout the body reflecting glucose utilization by the different tissues.

The basis of PET is, therefore, that the pharmaceutical or substrate interacts with the body through a metabolic process; the radionuclide allows that interaction to be followed, mapped, and measured. For medical applications of PET, the most important radionuclides, with half-lives in parentheses, are ^{15}O (2.03 min), ^{13}N (9.96 min), ^{11}C (20.4 min), and ^{18}F (109.8 min). For clinical applications, ^{18}F is currently of greatest importance in oncology due to the widespread use of FDG. The maximum energy of the positron from decay of ^{18}F is 0.633 MeV, with a mean range of 0.6 mm. It is, therefore, a nuclide with favorable properties for high-resolution PET imaging.

Spatial Resolution

The physics of positron emission imposes certain limitations on the spatial, temporal, and contrast resolution that can be attained in a particular imaging situation. Positron range (see Figure 1.1a) is obviously one limitation on the spatial resolution, because the goal is to map the distribution of positron-emitting nuclei and not the distribution of annihilation points. The energy carried by the positron may not be entirely dissipated during its journey in tissue, and the annihilating electron-positron system may have residual momentum. To conserve momentum, the annihilation photons are emitted slightly less than 180° apart, further contributing to a loss of spatial resolution because the two photons are assumed to be collinear and to form a straight line containing the point of emission of the positron. Neither of these assumptions is exact, and both positron range and acolinearity of the photons degrade spatial resolution. The contribution from acolinearity increases with increased separation of the coincident detectors, and the resolution degradation is a maximum at the center of the transverse field of view. For typical whole-body PET scanner designs, the contribution from photon acolinearity will be about 1.5 mm full-width at half-maximum (FWHM) for ^{18}F. Although these physical effects place a lower limit on the spatial resolution that can be achieved with PET, contributions from the size and design of the PET detectors further degrade the spatial

resolution in clinical PET scanners. Physical effects contribute 2 mm or less, whereas the spatial resolution of a PET scanner in a clinical imaging situation is, at best, about 6 mm.

Scatter and Randoms

As with any imaging technique, not all acquired events contribute to the signal. Contributions to background noise include photons that scatter before detection and photons from two unrelated annihilations that are erroneously assigned to a single positron emission, as shown schematically in Figure 1.2. For scattered events (Figure 1.2a), one or both photons interact in the tissue before reaching the detectors and as a consequence the event is assigned incorrectly to the line joining the two detectors. The level of scatter, which at this energy is primarily caused by Compton scattering, is characterized by the scatter fraction (SF), the ratio of scattered to total events. Random coincidences (Figure 1.2b) are photon pairs from uncorrelated positron annihilations that arrive within the electronic time window (2τ) that defines a coincidence. The random coincidence rate increases linearly with the width of the time window and quadratically (except at very low rates) with the rate of single photons interacting in the detectors. Both these background processes introduce a bias into the reconstructed images, a bias that can be reduced or eliminated by measuring or modeling each process, although usually at the expense of increasing image noise.

Scattered photons can, in principle, be identified from the energy lost in the scattering process and rejected by applying a simple energy threshold. However, as seen later, the energy resolution of current PET detectors is unable to accurately distinguish scattered from nonscattered photons above a certain energy threshold that may be as low as 350 keV for BGO detectors. Thus, in addition to a lower energy threshold, sophisticated scatter correction models have been developed to remove the residual scatter bias (10–12). The scatter background cannot be measured directly and must, instead, be estimated from the data. In a typical clinical imaging situation, even after applying an energy threshold, the fraction of the total events in the image that are scattered (SF) is 8%–10% in two dimensions (2D) and up to 45% or greater in three dimensions (3D).

As mentioned, the random coincidence rate (R) is proportional to the square of the radiation (singles rate) incident on the detectors. This radiation arises not only from the radioactivity in the field of view of the scanner, but also from radioactivity outside the field of view when one of the two photons from a given positron annihilation enters the scanner field-of-view and reaches the detectors. For whole-body clinical imaging with FDG, the radiopharmaceutical distributes throughout the body and radioactivity that localizes in regions not within the field-of-view of the scanner increases the overall randoms rate to a level that may exceed 50% of the total acquisition rate. The randoms rate can be estimated from the singles rate and the coincidence time window (Figure 1.2b), or from a direct measurement of delayed events acquired in an out-

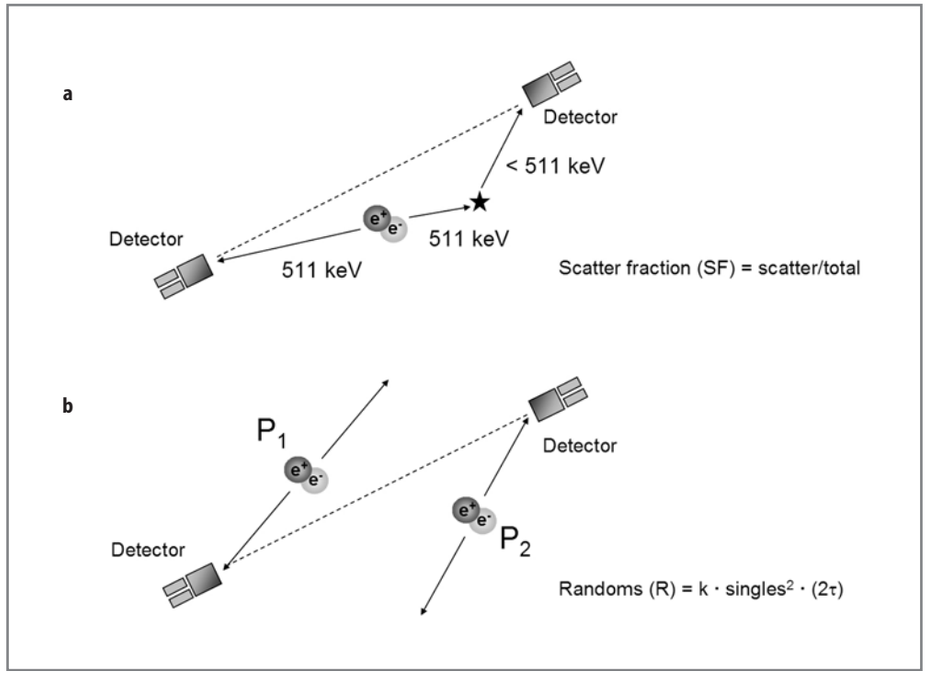

Figure 1.2. Contributions to PET data, acquired in addition to the true coincidences, where (**a**) one (or both) photons scatter and lose energy before they reach the PET detectors and (**b**) two annihilation photons from different positron decays, P_1 and P_2, are detected within the coincidence time window (2τ) appearing to form a true coincidence; such events are termed random coincidences.

of-time window. The advantage of a direct measurement of randoms is that it can account for any spatial variations in the distribution, whereas the disadvantage is that, as a measurement, it increases image noise when the randoms are subtracted.

Attenuation and Attenuation Correction

Annihilation photons that scatter are not only assigned to the incorrect line-of-response (LOR) (see Figure 1.2a), but they are also removed from the correct LOR. The removal of annihilation events from an LOR, either by Compton scattering or photoelectric absorption, is termed attenuation, as shown schematically in Figure 1.3a. Attenuation of 511-keV photons follows the usual exponential absorption law determined by the linear attenuation coefficient $\mu(x, E)$, where x is the pathlength in tissue and E is the photon energy; for PET, E = 511 keV, the rest mass of the positron or electron. A well-known advantage of PET is that, because *both* annihilation photons must traverse the tissue without interaction, attenuation is depth independent and is a function of the total thickness of tissue, greatly simplifying the attenuation correction procedure compared to SPECT. The attenuation correction factor (ACF) for a given LOR is obtained by integrating the linear attenuation coefficients along the path of the LOR (Figure 1.3a). The limits of integration, x_1 and x_2, are coordinates, measured along the LOR (k), at the entrance and exit of the patient. For PET, the correction is (1) independent of source depth, and (2) exact, since the ACFs can be measured directly (Figure 1.3b). The measurement is analogous to a CT scan acquired at 511 keV, rather than at 70 keV as in clinical CT. Up to three ^{68}Ge rod sources (R) covering the full axial extent of the scanner circulate around the patient to acquire the corresponding transmission data at 511 keV. The total transmission counts, I(k), acquired for a given LOR k is compared to the nonattenuated counts, $I_0(k)$, acquired in the absence of a patient (blank scan), and the ratio $I_0(k)/I(k)$ yields the ACF for LOR k. By measuring this ratio for all LORs, and applying the factors to the PET emission data, the effect of attenuation can be corrected.

For PET, the attenuation correction procedure is, in principle, exact. However, because the correction is based on a measurement involving photon counting statistics, additional noise is introduced into the PET data. The radioactivity in the rod sources is limited to avoid excessive dead time in adjacent PET detectors, and transmission scan times may represent 40% or more of the total scan duration.

For whole-body imaging of large patients, the ACFs are significant, exceeding a factor of 300 for LORs through the shoulders and abdomen, thereby amplifying the intrinsic noise in the PET emission data. Despite this noise amplification, the importance of correcting for attenuation in whole-body FDG scans is evident, as shown in Figure 1.4, comparing the uncorrected image (Figure 1.4a) and the corrected image (Figure 1.4b). Artifactually increased uptake in the skin and lungs, as well as nonuniform recovery of uptake in the liver and spleen, are well-known features of uncorrected FDG-PET images. The uncorrected images are not quantitative and, for interpretation purposes, estimates of standardized uptake values (SUVs) will be inaccurate.

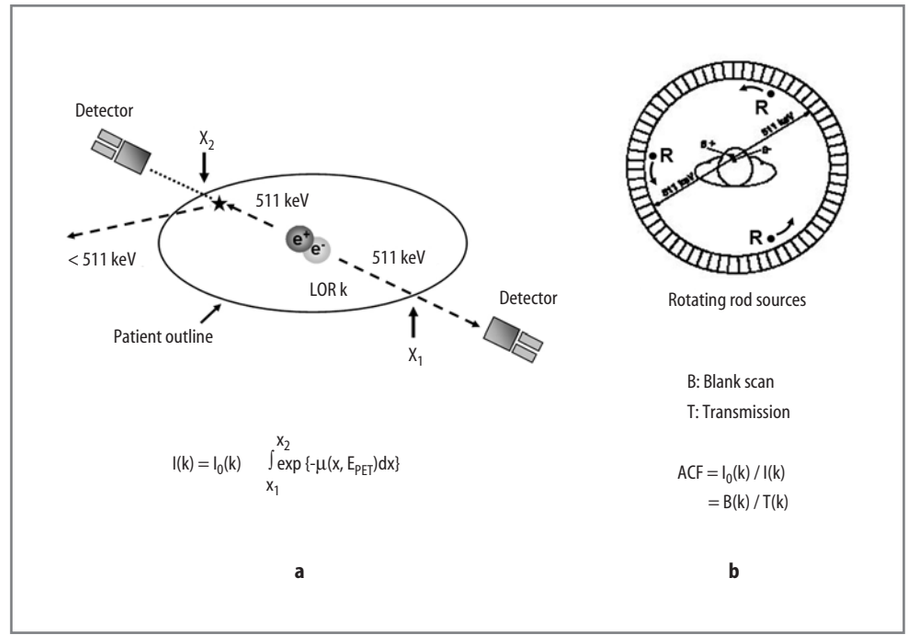

Figure 1.3. The physics of PET attenuation and a procedure for correction of the attenuation effect. (**a**) An annihilation photon scatters in the patient, and the event is removed from that line-of-response (k). The attenuated activity I(k) is given by the unattenuated activity $I_0(k)$ multiplied by the integral along the LOR k of the linear attenuation coefficient $\mu(x, E_{PET})$ at the PET energy (511 keV). The integration variable x is integrated from x_1 to x_2, the limits of the intersection of the LOR k with the outline of the patient. (**b**) To correct for attenuation, the unattenuated activity $I_0(k)$ for LOR k is estimated from a blank scan B(k) acquired in the absence of a patient with up to three rotating rod sources (R) of ^{68}Ge. The attenuated value I(k) is obtained from the transmission scan T(k) acquired with the patient positioned in the scanner. The attenuation correction factor ACF for each line of response (LOR) k is given by the ratio B(k)/T(k).

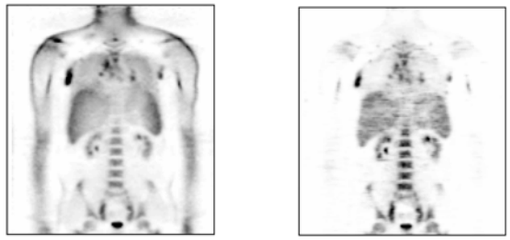

a b

Figure 1.4. A coronal section through a whole-body FDG-PET image of a patient: the images have been reconstructed (**a**) without correction for attenuation and (**b**) with correction for attenuation, obtained as described in Figure 1.3. Note in the uncorrected image (**a**) the artifactual appearance of increased activity in the lungs, skin, and periphery of the liver as compared to the corrected image (**b**).

Imaging Technology for PET

The past decades has witnessed significant advances in the imaging technology available for PET, the pace increasing recently with the introduction of new fast scintillators and the combination of anatomic and functional imaging within the same scanner. This section briefly reviews some of these developments in PET imaging technology, including the basic block detector design, scintillator performance, two-dimensional (2D) and three-dimensional (3D) imaging, and reconstruction algorithms. Combined anatomic and functional imaging are discussed in the subsequent section.

PET Detectors

The PET block detector was first developed by Casey and Nutt in the mid-1980s (13). Previous efforts to improve PET spatial resolution through the use of smaller scintillation detectors, each coupled to a photomultiplier tube, became prohibitively expensive. In addition, the demand to increase the axial coverage of PET scanners by incorporating multiple detector rings into the design created complex and inconvenient coupling schemes to extract the scintillation signals. Multiplexing first 32, and then 64, detectors to four phototubes, Casey and Nutt decreased both complexity and cost in one design (13). A block of scintillator is cut into 8 x 8 detectors and bonded to four photomultipliers (Figure 1.5). Light sharing between the four phototubes (A to D) is used to localize the detector element in which the incident photon interacts. The block design shown in Figure 1.5 has been the basic detector component in all multiring PET scanners for more than 17 years.

Scintillators for PET

The first PET scanners, developed in the 1960s and early 1970s, were based on various geometric configurations of

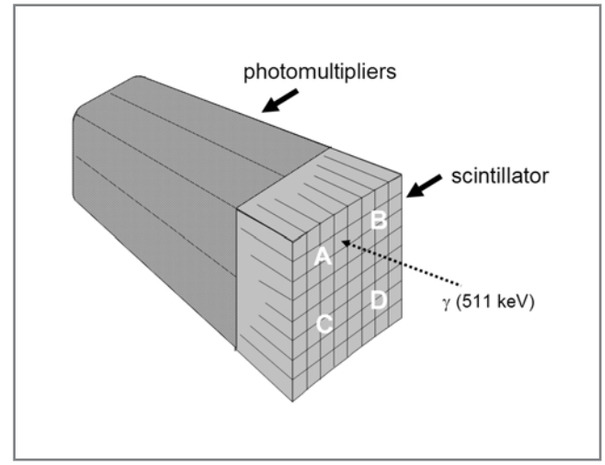

Figure 1.5. The concept of the PET block detector design. A block of scintillators is partitioned into 8 x 8 small elements with cuts of different depths. The scintillator is bonded to four photomultiplier tubes, A to D. An incident 511-keV annihilation photon is converted to light and detected by the phototubes. The distribution of light among the four phototubes localizes the position of the incident annihilation photon.

thallium-activated sodium iodide crystals [NaI(Tl)], a scintillator that is widely used in standard nuclear medicine gamma cameras to detect the 140-keV photons from the decay of technetium. To detect 511-keV annihilation photons, however, the low density of NaI(Tl) is a disadvantage unless thicker crystals are used to compensate for the reduced stopping power. In the late 1970s, bismuth germanate (BGO), a denser scintillator with greater stopping power than sodium iodide, was first considered as a prospective detector for PET (14). Compared to NaI(Tl), the higher density and increased photo fraction of BGO offer improved sensitivity by detecting a greater fraction of the incident photons. The light output of BGO is only about 15% of NaI(Tl) and the decay time is about 30% longer. Despite these suboptimal properties, BGO became established as the most widely used scintillator for PET for more than 25 years. Some of the physical properties of NaI(Tl) and BGO are compared in Table 1.1. Nevertheless, the use of NaI(Tl) for PET imaging continued and one company, UGM Medical (Philadelphia, PA, USA), successfully developed PET scanners based on NaI(Tl) crystals

Table 1.1. Physical properties of different scintillators for positron emission tomography (PET)

Property	NaI	BGO	LSO	GSO
Density (g/mL)	3.67	7.13	7.4	6.7
Effective Z	51	74	66	61
Attenuation length (cm)	2.88	1.05	1.16	1.43
Decay time (ns)	230	300	35–45	30–60
Photons/MeV	38,000	8,200	28,000	10,000
Light yield (%NaI)	100	15	75	25
Hygroscopic	Yes	No	No	No

NaI, sodium iodide; LSO, lutetium oxyorthosilicate; BGO, bismuth germanate; GSO, gadolinium oxyorthosilicate.

that were thicker than those used in the conventional gamma camera (15).

Thus, from the late 1980s, the BGO block detector became a standard for PET imaging. Blocks of scintillator 50 mm × 50 mm in size and 20 mm to 30 mm deep were cut into 8 × 8 crystals and bonded to four 1-inch photomultiplier tubes (Figure 1.5). Two contiguous rings of blocks covered an axial extent of 10 cm with 16 rings of crystals, each approximately 6 mm × 6 mm in size. A design with a third ring of blocks covering a total of 15 cm axially with 24 rings of detectors appeared in the early 1990s and became established as one of the most effective configurations for clinical PET scanning throughout the decade (16). The energy resolution and count rate performance of these multiring scanners were limited by the physical characteristics of BGO and thus a search for PET scintillators with improved characteristics was initiated, one that would have greater light output and shorter decay time than BGO.

The introduction of new, faster scintillators such as gadolinium oxyorthosilicate (GSO) (17) and lutetium oxyorthosilicate (LSO) (18), both doped with cerium, has recently improved the performance of PET scanners for clinical imaging. The physical properties of these newer scintillators are also compared in Table 1.1. Both GSO and LSO have shorter decay times than BGO by a factor of 6 to 7, reducing system deadtime and improving count rate performance, particularly at high activity levels in the field of view. Of even more importance for clinical imaging is the potential of faster scintillators to decrease the coincidence timing window, thereby reducing the randoms coincidence rate. The increased light output of the new scintillators improves the energy resolution because the increased number of light photons reduces the statistical uncertainty in the energy measurement. However, other physical effects contribute to the emission process and the improvement in energy resolution is not a simple function of the number of light photons. The increased light output also improves the positioning accuracy of a block detector (see Figure 1.5), presenting the possibility to cut the blocks even finer into smaller crystals, thus further improving spatial resolution. Unlike NaI(Tl), BGO, LSO, and GSO are not hygroscopic, facilitating the manufacture and packaging of the detectors. GSO is somewhat less rugged and more difficult to machine than either BGO or LSO. LSO has an intrinsic radioactivity of about 280 Bq/mL with single photon emissions in the range 88 keV to 400 keV. Such a radioactive component is of little consequence for coincidence counting at 511 keV, except possibly at very low count rates.

Imaging in 3D

PET is intrinsically a 3D imaging methodology, replacing the physical collimation required for single photon imaging with the electronic collimation of coincidence detection. However, the first multiring PET scanners incorporated septa, lead or tungsten annular shields mounted between the detector rings (Figure 1.6a). The purpose of the septa was to shield the detectors from photons that scattered out of the transverse plane, thus restricting the use of electronic collimation to within the plane. This restriction also allows 2D reconstruction algorithms to be used on a plane-by-plane basis rather than requiring a full 3D reconstruction algorithm. However, by restricting annihilation events to a set of 2D planes, inefficient use is made of the emitted radiation. When the septa are extended (Figure 1.6b), only LORs with small angles of incidence are active; the remaining LORs intersect the septa and the photons never reach the detectors. When the septa are retracted (Figure 1.6c), many more LORs are active and the overall scanner sensitivity increases by a factor of 6 or greater, depending on the exact design (19).

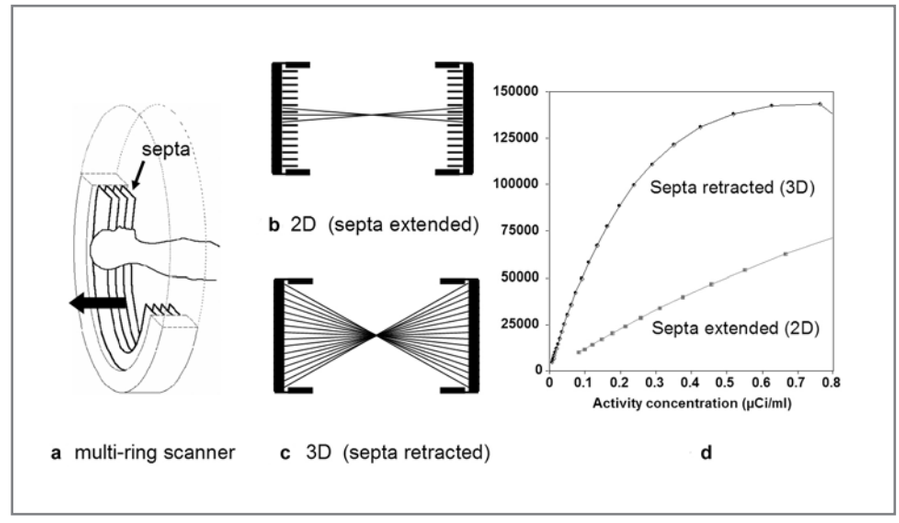

Figure 1.6. PET acquisition in 2D and 3D modes. (**a**) Schematic of a multiring PET scanner with interring lead septa to shield the detector rings from out-of-plane scatter and randoms. (**b**) With the septa extended into the field-of-view, the number of active LORs is limited to those in-plane and small incident angles, whereas with the septa removed (**c**) the number of active LORs is greatly increased, thereby improving the sensitivity. (**d**) The noise equivalent count rate (NECR) as a function of activity concentration in the field-of-view shows significantly improved performance in 3D mode with the septa retracted, particularly at lower activity concentrations.

The first multiring PET scanners with retractable septa that included the capability to acquire data in either 2D or 3D mode appeared in the early 1990s (20).

Because the scatter and randoms rates also increase when the septa are retracted, any estimation of the net benefit of 3D imaging compared to 2D imaging must take into account these increases, and not just the increase in true coincidence events. The scatter fraction, for example, increases by a factor of at least 3 compared to 2D imaging and randoms rates increase by a similar or greater factor (19). A measure of actual improvement in signal-to-noise is the noise equivalent count rate (NECR) (21), defined by the expression $T^2/(T + S + \alpha R)$, where T, S, and R are the true, scattered, and random coincidence rates, respectively. The improvement in signal caused by the increase in true counts (from retracting the septa) is offset by the increase in statistical noise on T, the scattered events S, and the randoms R, as expressed in the denominator of the NECR. The factor α equals 2 for online randoms subtraction from the delayed coincidence window and 1 for noiseless randoms subtraction. Smoothing the randoms before subtraction therefore corresponds to $1 < \alpha < 2$. The NECR is shown in Figure 1.6d as a function of activity concentration in a 20-cm-diameter uniform cylinder for 2D and 3D acquisition mode. The significant improvement in the 3D NECR, and hence signal-to-noise, at lower activity concentrations is evident from the graphs.

While the curves in Figure 1.6d highlight the benefits of 3D imaging for the brain, 3D imaging for the rest of the body has been more problematic, mainly because of the difficulty of shielding the detectors from activity in the body outside the imaging field-of-view when the septa are retracted. Recently, however, a number of factors have significantly improved the image quality that can be achieved for whole-body 3D imaging. These factors include advances in reconstruction algorithms, more accurate scatter correction, and the introduction of the new, faster scintillators described previously.

The progress in reconstruction has primarily been the introduction of statistically-based algorithms into the clinical setting. Previously, one of the earliest and most widely used 3D reconstruction algorithms was the reprojection approach based on a 3D extension of the original 2D, filtered backprojection algorithm (22). Although this algorithm works well for the lower noise environment of brain imaging, the quality for whole-body imaging is less than optimal (Figure 1.7a). The development of Fourier rebinning (FORE) (23) enabled 3D data sets to be accurately rebinned into 2D data sets and reconstructed in 2D with a statistically-based algorithm such as ordered-subset expectation-maximization (OSEM) (24). The result of applying OSEM to the same data set as in Figure 1.7a is shown in Figure 1.7b. The improvement in image quality compared with Figure 1.7a is significant, although some nonuniformity remains in the liver and spleen. Further progress has been made by incorporating attenuation information directly into the reconstruction model in the form of weighting factors (Figure 1.7c). The activity in the liver and spleen shows improved uniformity, and the overall image quality is superior with the use of FORE and attenuation-weighted OSEM (AWOSEM) (25). The FORE + AWOSEM approach is an example of a hybrid 3D algorithm, where the data are acquired in 3D, rebinned to 2D, and reconstructed with a 2D algorithm. Other similar combinations are possible, such as the "2.5-dimensional" row action maximum-likelihood algorithm (2.5D RAMLA) developed by Daube-Witherspoon et al. (26) and used for clinical imaging. A second advance that has contributed to the improved image quality in 3D whole-body imaging has been progress in scatter correction algorithms. In particular, the development of faster, image-based algorithms (27) has improved accuracy. The elevated levels of scatter encountered in 3D imaging can be accurately estimated from the emission and transmission data and subtracted from the reconstructed images. Finally, one of the most significant factors contributing to the adoption of 3D acquisition for clinical whole-body imaging has been the introduction of the new, faster scintillators described earlier. For LSO, in particular, a shorter coincidence time window, reduced dead time, and improved energy resolution compared to the corresponding BGO scanner increases the maximum NECR and improves signal-to-noise.

Imaging Technology for PET/CT

The development of the combined PET/CT scanner (3, 4, 28) is an evolution in imaging technology whereby the

a b c

Figure 1.7. An FDG-PET whole-body scan acquired in 3D mode with septa retracted and reconstructed using (**a**) 3D filtered back-projection algorithm with reprojection (Hann window: cutoff, 0.5; 6-mm Gaussian smooth; (**b**) FORE plus OSEM (8 subsets, 2 iterations; 6-mm Gaussian smooth); and (**c**) FORE plus AWOSEM (8 subsets, 2 iterations; 6-mm Gaussian smooth). (These reconstructions were provided by Dr. David Brasse, now at the Institut de Recherches Subatomique, Strasbourg, France.)

Table 1.2. Some drawbacks of software fusion resolved by the hardware approach.

Software fusion	Hardware fusion
Access to image archives required	Images immediately available
Carefully controlled patient positioning	Single-patient positioning
Different scanner bed profiles	Same bed for both scans
Internal organ movement	Little internal organ movement
Disease progression in time	Scans acquired close in time
Limited registration accuracy	Improved registration accuracy
Inconvenience for patient (2 scans)	Single, integrated scan
Labor-intensive registration algorithms	No further alignment required

fusion of two established modalities becomes greater than the sum of the individual parts. It is well known, of course, that CT and PET scans of the same patient acquired on different scanners can be aligned using a number of available software methods (9, 29–31), even though the algorithms are often labor intensive and, outside the brain, may fail to converge to a satisfactory solution. An alternative approach, therefore, is to combine the imaging technology of CT and PET into one scanner such that both anatomy and function, accurately aligned, are imaged in a single scan session. This approach has been termed the hardware fusion approach. Some of the drawbacks of the software approach and the way in which they are addressed by the recently developed hardware approach are summarized in Table 1.2. Of particular importance is the positioning of the patient, the use of the same bed for both scans, and minimization of the effect of uncontrollable internal organ movement. For nonspecific tracers, such as FDG with normal, benign accumulation in tissue and organs, it is important, especially in the abdomen and pelvic region, to distinguish normal uptake from disease. Because accurate localization is routinely available with combined PET/CT scanning, such a distinction is generally straightforward.

Design Objectives

The development of the first PET/CT prototype was initiated in 1992 with the objectives to integrate CT and PET within the same device, to use the CT images for the attenuation and scatter correction of the PET emission data, and to explore the use of anatomic images to define tissue boundaries for PET reconstruction. Thus, the goal was to construct a device with both clinical CT and clinical PET capability so that a full anatomic and functional scan could be acquired in a single session, obviating the need for the patient to undergo an additional clinical CT scan. The original prototype (4) combined a single-slice spiral CT (Somatom AR.SP; Siemens Medical Solutions) with a rotating ECAT ART scanner (CPS Innovations, Knoxville, TN, USA). The components for both imaging modalities were mounted on the same mechanical support and rotated together at 30 rpm. However, by the time the prototype became operational in 1998 (4), neither the CT nor the PET components were state-of-the-art. Nevertheless, the work convincingly demonstrated the feasibility of combining the two technologies into a single device that could acquire coregistered anatomic and functional images without the need for software realignment.

As mentioned, a number of important lessons emerged during the clinical evaluation program that followed the installation of the prototype and covered the years from 1998 until 2001 (5–8). More than 300 cancer patients were scanned, and the studies highlighted the advantages of being able to accurately localize functional abnormalities, to distinguish normal uptake from pathology, to minimize the effects of both external and internal patient movement, and to reduce scan time and increase patient throughput by using the CT images for attenuation correction of the PET data. Even during the initial evaluation it was evident that coregistered anatomy increases the confidence of physicians reading the study. Radiologists rapidly came to appreciate that coregistered functional images help to focus attention on regions of abnormal uptake, especially regions with no evident pathology on CT.

Despite concerns over the likely cost and operational complexity of combined PET/CT technology, the major vendors of medical imaging equipment nevertheless recognized a market for PET/CT. The first commercial design comprised a CT scanner and a PET scanner enclosed within a single gantry cover and operated from separate consoles. The design involved little integration at any level and was intended primarily to be the first commercial PET/CT scanner on the market, as indeed it was. The PET scanner included retractable septa, and standard PET transmission sources were offered as an alternative to CT-based attenuation correction. Retractable septa allowed the device to acquire PET data in either 2D or 3D mode. Within a few months, another PET/CT design (Figure 1.8) from a different vendor appeared that had no septa and acquired data fully in 3D (32). Because no mechanical storage was required for retractable septa and standard PET transmission sources were not offered, the design was compact; the patient port was a full 70-cm diameter throughout, and the overall tunnel length was only 110 cm. Integration of the control and display software allowed the scanner to be operated from a single console. As with these and most subsequent commercial designs, both the CT and the PET were clinical state-of-the-art systems, following the objectives of the original prototype. A more open concept PET/CT with spacing between the CT and PET scanners has since been offered by two other vendors, allowing greater access to the patient and reducing possible claustrophobic effects of the other designs.

The hardware integration of recent PET/CT designs has, therefore, remained rather minimal. The advantage is that vendors can then benefit more easily from separate advances in both CT and PET instrumentation. In the past

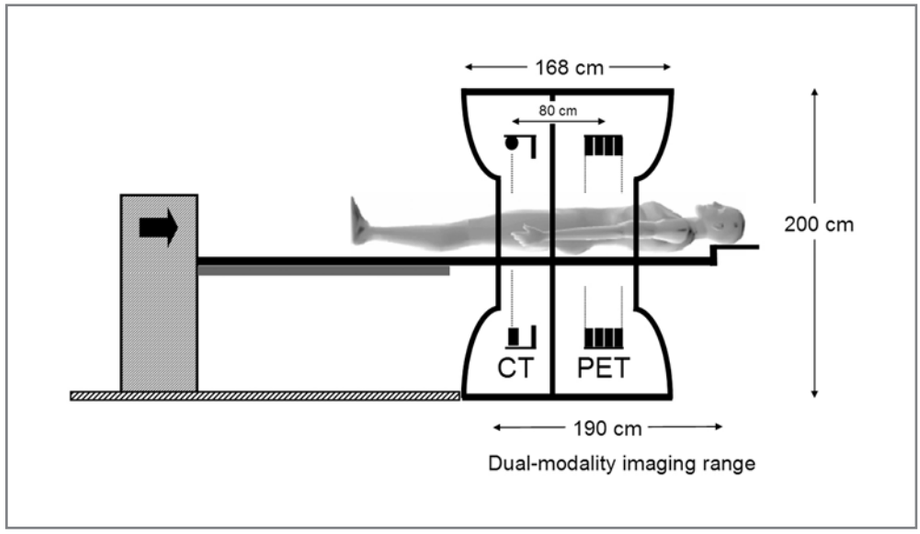

Figure 1.8. A schematic of a current PET-CT scanner design marketed by Siemens as the biograph (Siemens Medical Solutions, Chicago, IL, USA). The design incorporates a multidetector spiral CT scanner and a lutetium oxyorthosilicate (LSO) PET scanner. The dimensions of the gantry are 228 cm wide, 200 cm high, and 168 cm deep. The separation of the CT and PET imaging fields is about 80 cm. The co-scan range for acquiring both CT and PET is up to 190 cm. The patient port diameter is 70 cm.

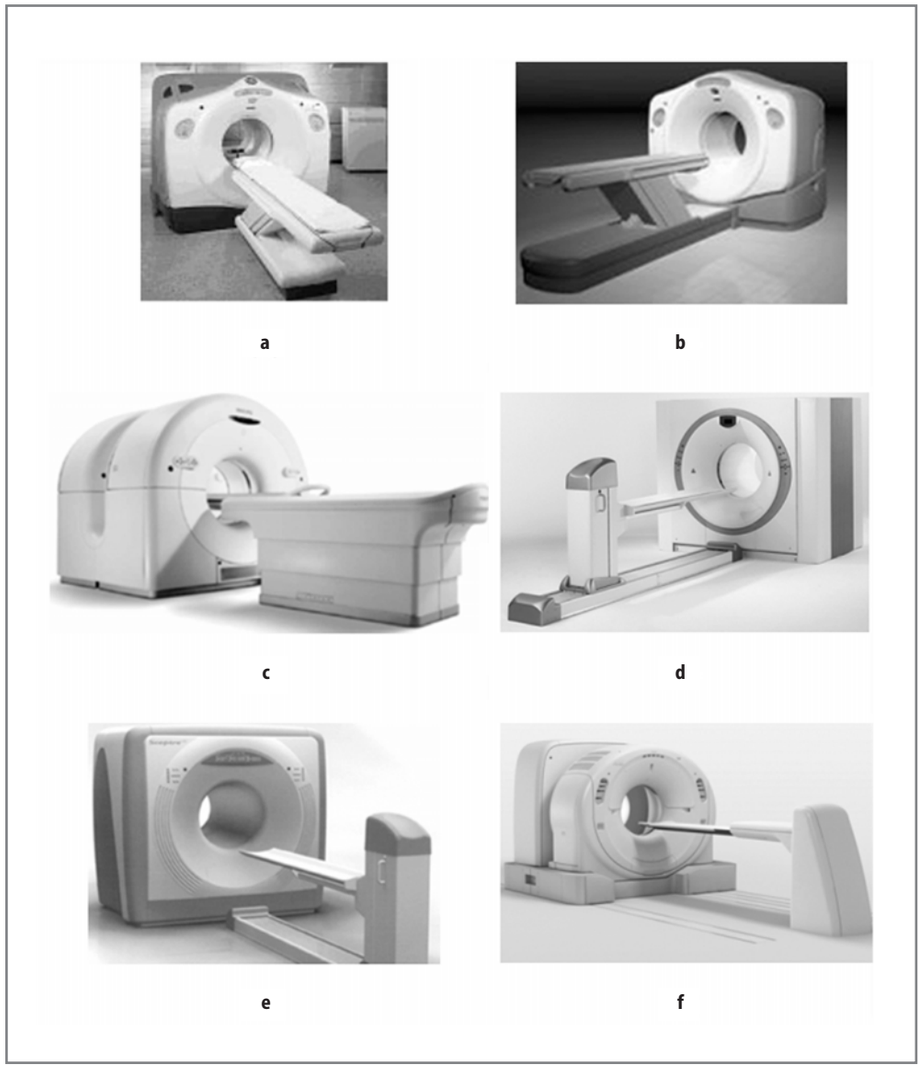

Figure 1.9. Current commercial PET/CT scanners from five major vendors of medical imaging equipment: (**a**) Discovery LS (GE Healthcare); (**b**) Discovery ST (GE Healthcare); (**c**) Gemini (Philips Medical Systems); (**d**) biograph (Siemens Medical Solutions); (**e**) SeptreP3 (Hitachi Medical Systems); (**f**) Aquiduo (Toshiba Medical Corporation).

few years, spiral CT technology has progressed from single to dual-slice, to 4, 8, 16, and, most recently, 64 slices; in parallel, CT rotation times have deceased to less than 0.4 s, resulting in very rapid scanning protocols. Advances in PET technology (as described earlier) have been equally dramatic with the introduction of the new faster scintillators GSO and LSO, faster acquisition electronics, and higher resolution detectors (smaller pixels). Currently, a top-of-the-line PET/CT configuration would comprise a 64-slice CT scanner and an LSO-based PET scanner with 4-mm pixels. However, although the 64-slice CT configuration is targeted primarily for cardiac applications, the greatest impact of PET/CT to date has been in the oncology field for which a 16-slice CT scanner is generally considered adequate.

Current Technology for PET/CT

Currently, five vendors offer PET/CT designs: GE Healthcare, Hitachi Medical, Philips Medical Systems, Toshiba Medical Corporation, and Siemens Medical Solutions. With the exception of the SceptreP3 (Hitachi Medical; Figure 1.9e), which is based on a 4-slice CT and rotating LSO detectors, all vendors offer a 16-slice CT option for higher performance, with some vendors also offering lower-priced systems with 2-, 4-, 6-, or 8-slice CT detectors. The specifications and performance of the PET components are vendor specific, with the biograph HI-REZ (Siemens Medical Solutions; Figure 1.9d) offering the best overall spatial resolution in 3D with 4 mm × 4 mm LSO crystals; the original biograph design was based on 6 mm × 6 mm LSO detectors. The biograph is offered with 2-, 6-, 16-, and now 64-slice CT scanners. The same HI-REZ PET detectors are incorporated into the Aquiduo (Toshiba Medical; Figure 1.9f) in combination with the 16-slice Aquillion CT scanner (Toshiba Medical); a unique feature of this device is that the bed is fixed and the CT and PET gantries travel on floor-mounted rails to acquire the CT and PET data. The CT and PET scanners in the Aquiduo can be moved separately, and this is the only PET/CT design in which the CT tilt option has been preserved. The Discovery LS, the original PET/CT design from GE Healthcare, combined the Advance NXi PET scanner with a 4- or 8-slice CT (Figure 1.9a); note the size difference between the smaller CT scanner in front and the larger Advance PET scanner at the rear. The more recent Discovery ST from GE Healthcare has 6 mm × 6 mm BGO detectors in combination with a 16- or 64-slice CT scanner (Figure 1.9b); the gantry of the newly designed PET scanner now matches the dimensions of the CT scanner. The Gemini GXL (Philips Medical; Figure 1.9c) comprises 4 mm (in plane) and 6 mm (axial) GSO detector pixels, 30 mm in depth; the Gemini is also an open design with the capability to physically separate the CT and PET scanners for access to the patient, as in the Aquiduo. Each vendor has adopted a unique design for the patient couch to eliminate vertical deflection of the pallet (Figure 1.10) as it advances into the tunnel during scanning. All designs other than the SceptreP3 and the Discovery LS offer a 70-cm patient port for both CT and PET, thus facilitating the scanning of radiation therapy

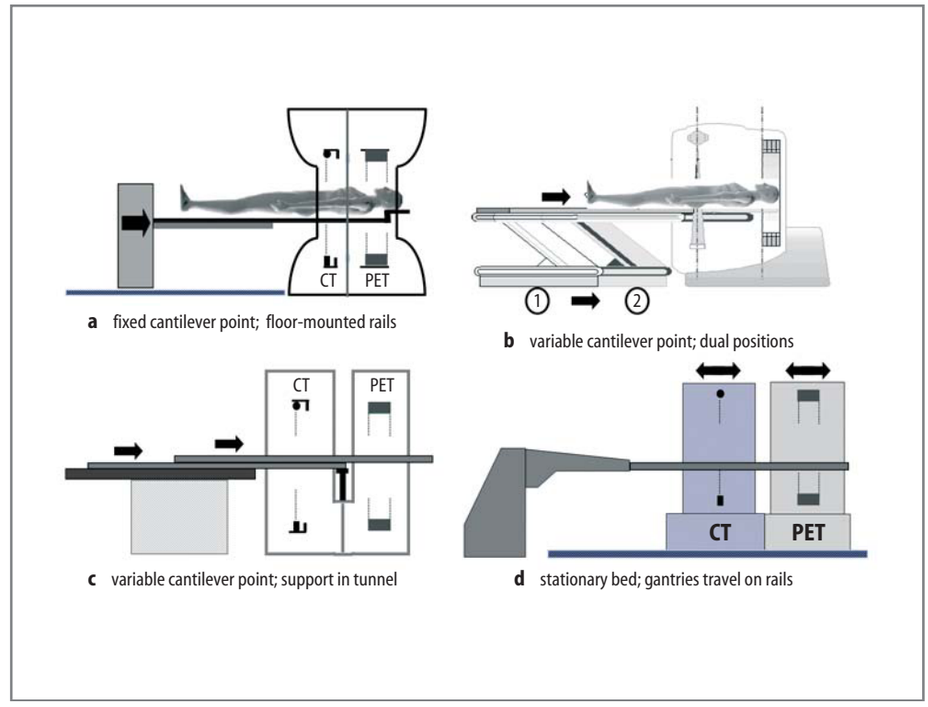

Figure 1.10. Four different solutions to the patient handling system (PHS) that eliminate variable vertical deflection of the pallet as it advances into the tunnel of the scanner. The designs include (**a**) a bed with a fixed cantilever point where the entire couch assembly moves on floor-mounted rails (biograph and SeptreP3), (**b**) a dual-position bed with one position for CT and one for PET (Discovery LS and ST), (**c**) a patient couch that incorporates a support throughout the tunnel (Gemini), and (**d**) a fixed couch with the scanner traveling on floor-mounted rails (Aquiduo).

patients in treatment position. Although the Discovery and Gemini also offer standard PET transmission sources as an option, in practice most institutions use CT-based attenuation correction because of the advantage of low noise and short scan times that facilitate high patient throughput.

The Gemini, SceptreP3, Aquiduo, and biograph designs acquire PET data in 3D mode only, whereas the Discovery incorporates retractable septa and can acquire data in both 2D and 3D mode. While the debate continues as to whether 2D or 3D acquisition yields better image quality, particularly for large patients, significant improvement in 3D image quality has undoubtedly been achieved through the use of faster scintillators and statistically based reconstruction algorithms. The scintillators GSO (Gemini) and LSO (SceptreP3, Aquiduo, and biograph) result in lower rates of both scattered photons and random coincidences compared to BGO and offer superior performance for 3D whole-body imaging.

Although there has, to date, been little actual effort to increase the level of hardware integration, there has been significant effort to reduce the complexity and increase the reliability of system operation by adopting a more integrated software approach. In early designs, CT and PET data acquisition and image reconstruction were performed on separate systems accessing a common database. Increasingly, functionality has been combined so as to reduce cost and complexity and increase reliability. Similar considerations of cost and complexity for the hardware may lead, in the future, to greater levels of integration. The likelihood is that these designs will be application specific, incorporating an 8- or 16-slice CT for oncology and a 64-slice CT for cardiology. There will undoubtedly be a demand for more cost-effective, entry-level PET/CT designs for oncology such as the Hitachi SceptreP3, with the likelihood that PET/CT will eventually replace PET-only scanners entirely.

Even though all PET/CT designs offer clinical quality CT and PET, many centers elect to operate with low-dose, nondiagnostic CT for attenuation correction and localization only. This approach does not therefore use the PET/CT to its full, clinical potential, and it is hoped that, as PET/CT is introduced more widely into clinical routine, direct referrals for PET/CT will increase. With more than 1,000 PET/CT scanners installed worldwide, PET/CT now represents more than 95% of all PET sales and more than 10% of CT sales. In the 4 years since the first commercial PET/CT was introduced, the modality has had a far-reaching impact on medical imaging, particularly for staging malignant disease and monitoring response to therapy.

CT-Based Attenuation Correction

The acquisition of accurately coregistered anatomic and functional images is obviously a major strength of the combined PET/CT scanner. However, as mentioned, an additional advantage of this approach is the possibility to use the CT images for attenuation correction of the PET emission data, eliminating the need for a separate, lengthy PET transmission scan. The use of the CT scan for attenuation correction not only reduces whole-body scan times by at least 40%, but also provides essentially noiseless ACFs compared to those from standard PET transmission measurements. Because the attenuation values are energy dependent, the correction factors derived from a CT scan at mean photon energy of 70 keV must be scaled to the PET energy of 511 keV. The CT photon energy represents the mean energy of the polychromatic X-ray beam.

Scaling algorithms typically use a bilinear function to transform the attenuation values above and below a given threshold with different factors (33, 34). The composition of biologic tissues other than bone exhibit little variation in their effective atomic number and can be well represented by a mixture of air and water. Bone tissue does not follow the same trend as soft tissue because of its calcium and phosphorus content, and thus a different scaling factor is required that reflects instead a mixture of water and cortical bone. The breakpoint between the two mixture types has been variously set at 300 Hounsfield units (HU) (33) and at 0 HU (34). However, some tissue types, such as muscle (~60 HU) and blood (~40 HU), have Hounsfield units greater than zero and yet are clearly not a water–bone mix. A breakpoint around 100 HU would therefore appear to be optimal (Figure 1.11). Hounsfield units define the linear attenuation coefficients normalized to water and thus independent of the kVp of the X-ray tube. The scale factor for the air–water mix below about 100 HU will be independent of the kVp of the tube; this does not apply to the water–bone mixing and therefore the scale factor for bone is kVp dependent (35). The scaled CT images are then interpolated from CT to PET spatial resolution and the ACFs generated by reprojection of the interpolated images.

Intravenously injected iodinated contrast is used in CT to enhance attenuation values in the vasculature by increasing the photoelectric absorption compared with blood and resulting in a 40% change in attenuation. At the PET energy, where the photoelectric effect is negligible, the presence of contrast has only a 2% effect on attenuation. However, if contrast-enhanced pixels are misidentified as a water–bone mix, the scaling factor will be incorrect and the erroneously scaled pixels may generate artifacts in the PET image. Many thousands of PET/CT scans have now been performed in the presence of intravenous contrast, and experience has shown that contrast administration does not generally cause a problem that could potentially interfere with the diagnostic value of PET/CT (36). Oral contrast is administered to visualize the gastrointestinal tract and the distribution of the contrast material is rather variable, both in spatial distribution and in level of enhancement. Modifications to the basic scaling algorithm have been introduced to distinguish oral contrast enhancement from bone (37), and

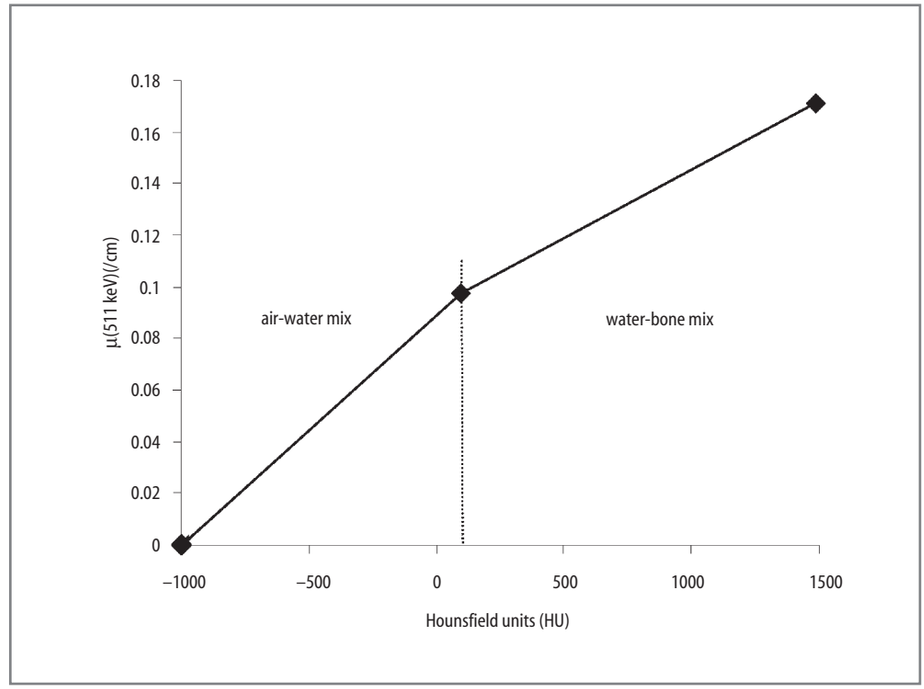

Figure 1.11. The bilinear scaling function used to convert CT numbers to linear attenuation values at 511 keV. The graph shows the linear attenuation coefficient at 511 keV as a function of the corresponding CT value (Hounsfield units, HU), based on measurements made with the Gammex 467 electron density CT phantom using tissue-equivalent materials. The separation between soft tissue (air–water mixing model) and bonelike tissue (water–bone mix) is about 100 HU.

strategies discussed elsewhere (38, 39) have been developed that minimize or eliminate problems from both intravenous and oral contrast. The modified algorithm (37) can, to some extent, also reduce artifacts caused by catheters and metallic objects in the patient. A more-detailed discussion of artifacts arising from metallic objects can be found elsewhere (40, 41).

Avoiding the administration of contrast would, of course, eliminate all such problems. However, standard-of-care in CT dictates the use of either intravenous or oral contrast, or both as in the case of the abdomen and pelvis. An obvious way to avoid such problems is to perform two CT scans: a clinical CT with appropriate contrast administration, and a low-dose, noncontrast CT for attenuation correction and coregistration. This two-scan approach, however, would further increase the radiation exposure to the patient.

PET/CT Protocols

Data acquisition protocols for PET/CT can, depending on the study, be relatively complex, particularly when they involve a clinical CT and a clinical PET scan. During the past 4 years since PET/CT technology first became commercially available, the initial rather simple and basic protocols have progressively become refined to correspond to accepted standards-of-care. Imaging protocols for oncology and cardiology are continuing to be refined and validated, and it will be some time before they become as well established as the corresponding protocols for CT only. Issues of respiration, contrast media, operating parameters, scan time, optimal injected dose of FDG, and others must be carefully addressed before definitive PET/CT protocols for specific clinical applications emerge. Nevertheless, there are certain common features to the protocols, as shown schematically in Figure 1.12, which illustrates a typical PET/CT scan.

As for any FDG-PET scan, following an injection of 370–550 M of FDG and a 90-min uptake period, the patient is positioned in the scanner. A 90-min uptake period is preferred over a 60-min period because increased washout of background activity and improved tumor-to-background ratios are obtained even though a longer time is allowed for decay of the radionuclide. For all studies other than head and neck cancer, the patient is positioned in the scanner with the arms up to reduce attenuation that results from having the arms in the field-of-view; for head and neck cancer, the scan is acquired with arms down. The first step in the study (see Figure 1.12a) is the acquisition of a topogram, or scout scan, which takes 10 to 15 s and covers a range of up to 200 cm. The total range to be scanned by both PET and CT is then defined on the topogram, based on the specific indication for the study (that is, skull base to abdomen for head and neck malignancies, and neck through upper thigh for most other malignancies; for melanoma, the scan range covers head to toe, whenever possible). An appropriate respiration protocol must be defined and implemented to minimize the mismatch between CT and PET. In the absence of respiratory gating (42, 43), a good match is found if the CT is acquired with partial or full expiration and the PET with shallow breathing. This approach is feasible with the 16-slice CT scanner where a scan of the thorax and abdomen

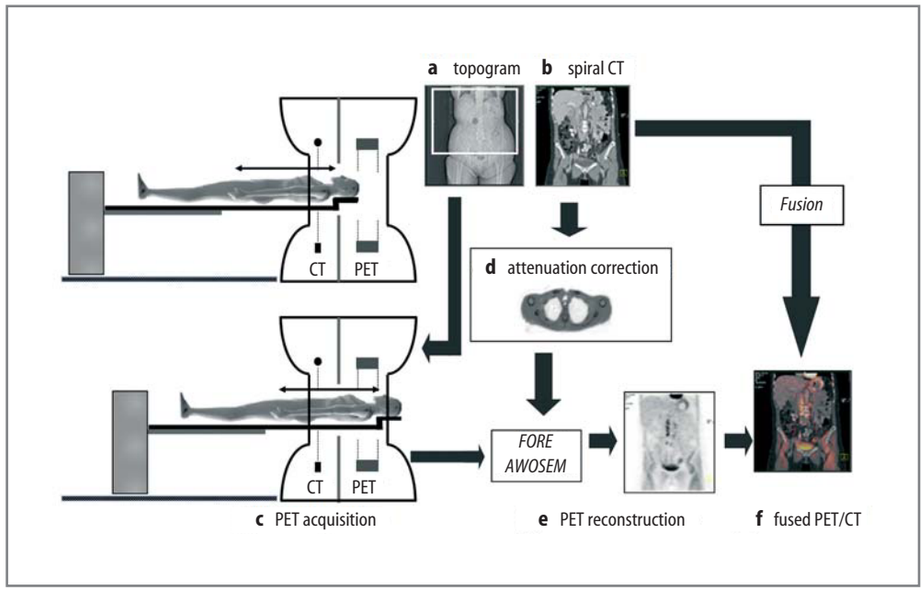

Figure 1.12. A typical imaging protocol for a combined PET/CT study that comprises (**a**) a topogram, or scout scan, for positioning; (**b**) a spiral CT scan; (**c**) a PET scan over the same axial range as the CT scan; (**d**) the generation of CT-based ACFs; (**e**) reconstruction of the attenuation-corrected PET emission data; and (**f**) display of the final fused images.

can be as short as 12 seconds. Problems posed by respiration mismatch have been discussed (44). The whole-body CT scan is usually acquired with a slice width of about 5 mm, which may not always correspond to standard clinical protocols. In some studies such as head and neck, a slice width of 3 mm may be preferred.

Upon completion of the spiral CT scan (Figure 1.12b), the patient couch is advanced into the PET field-of-view and a multibed PET scan acquired over the same range as the CT (Figure 1.12c). When the emission data are acquired in 3D, consecutive imaging fields typically overlap by 25% to average out the variations in signal-to-noise that would otherwise result. The reconstruction of the CT images occurs in parallel with the acquisition of the PET data, allowing the calculation of scatter and attenuation correction factors to be performed during the PET acquisition. The CT-based ACFs are calculated as described earlier (Figure 1.12d), and once the acquisition for the first bed position is completed, PET reconstruction can begin (Figure 1.12e). the 3D reconstruction is performed using Fourier rebinning (FORE) (23) and the attenuation-weighted ordered-subset algorithm (AWOSEM) (25) mentioned previously. Thus, within a few minutes of the acquisition of the final PET bed position, attenuation-corrected PET images are reconstructed and available for viewing, automatically coregistered with the CT scan by simply accounting for the axial displacement between the CT and PET imaging fields-of-view (Figure 1.12f). The fused image is displayed as a combination of the individual CT and PET image pixel values v_{CT} and v_{PET}, respectively. Using an alpha blending approach, the fused image pixel value (v) is given by $\alpha v_{CT} + (1 - \alpha)v_{PET}$; for $\alpha = 0$, the fused image is PET, whereas for $\alpha = 1$ the fused image is CT. Obviously, for $0 < \alpha < 1$, the fused image represents the weighted combined pixel values of CT and PET.

Although it is not feasible with current designs to acquire the CT and PET data simultaneously, scan times have been reduced significantly by the replacement of the lengthy PET transmission scan with the CT scan. In addition, as mentioned previously, the introduction of new PET technology such as faster scintillators (LSO and GSO) has reduced the emission acquisition time so that whole-body PET/CT acquisition times of 5 to 10 min are feasible with state-of-the-art systems (45). Shorter imaging times lead to higher patient throughput, potentially creating logistical problems for imaging centers. To maintain high throughput, injection times must be carefully coordinated to ensure the constant availability of patients after a 90-min (±5 min) uptake period. It is essential to provide an adequate number of injection and uptake rooms.

In addition to the issues related to respiration (42, 43) and contrast (38, 39), a topic of ongoing debate is the clinical role of the CT scan. Obviously a low dose (40 mAs) CT scan would be adequate for attenuation correction and localization, whereas a full-dose CT scan (130 mAs) is required for clinical purposes. The decision to acquire a clinical CT scan depends on many factors, including whether such a scan was ordered by the referring physician, whether the patient has recently had a clinical CT, and whether the scan will be reviewed by a radiologist when the PET/CT study is read. Obviously the decision, which may be application specific, will dictate the protocol and the parameters of the CT scan. Increasingly, as PET/CT becomes established in clinical routine, the acquisition of both a clinical CT and a clinical PET scan should become standard practice. Referring physicians will be advised to consider a PET/CT immediately rather than ordering first a CT that might be equivocal and then requiring a PET scan. Such an approach will ensure the best use is made of costly imaging equipment. More details on

these and other practical issues can be found in Coleman et al. (46).

Finally, although there are many technical reasons to prefer the combined PET/CT approach over software image fusion (see Table 2.2), the convenience to both patient and physician should not be underestimated. For the patient, one appointment and a single scan session is required to obtain complete anatomic and functional information related to his or her disease. For the physician, the potential to have accurately registered CT and PET images available at the same time and on the same viewing screen offers unique possibilities. The added confidence in reading and interpreting the study comes from the accurate localization of tracer accumulation, the distinction of normal uptake from pathology, and the verification that a suspicious finding can be confirmed by the other modality. In some cases, such a suspicious finding on one modality invites a closer examination of the other modality, a retrospective image review that can take place immediately after the PET/CT scan has concluded.

Conclusions

Even though combined PET/CT scanners have been in production for only 4 years, the technology is undergoing rapid evolution. For PET, the introduction of new scintillator materials, detector concepts, and electronics is resulting in performance improvements in count rate, spatial resolution, and signal-to-noise. At the same time, the increasing number of detector rows and reduction in rotation time are transforming whole-body CT performance. The combination of high-performance CT with high-performance PET is a powerful imaging platform for the diagnosis, staging, and therapy monitoring of malignant disease. Although the PET scanners incorporated into current PET/CT designs are still offered by some vendors for PET-only applications, more than 95% of PET sales are now PET/CT, and the likelihood is that PET-only scanners will be replaced entirely by PET/CT in the future. It is expected that there will then be a demand for a design that offers less performance at less cost. To meet this demand, an entry-level or midrange PET/CT is required, possibly in a form similar to the original prototype with PET detectors mounted on the same rotating assembly as the CT. Because the performance of the PET components is the limitation on the overall imaging time, institutions requiring high throughput and large patient volumes will always demand the highest PET performance. Nevertheless, a 6- or 8-slice CT scanner should be adequate for most oncology applications, with a 16- or 64-slice CT appropriate for PET/CT applications in cardiology. As the current PET/CT technology becomes more widespread, appropriate future designs of this concept will doubtless emerge.

Acknowledgments

The author is grateful to his colleagues at the University of Tennessee Medical Center, the University of Pittsburgh, the University of Essen, Germany, and CPS Innovations, Knoxville, Tennessee who have contributed significantly to the development of the combined PET/CT scanner. The PET/CT prototype was developed jointly with CPS Innovations, Knoxville, TN and funded in part by a grant from the National Cancer Institute (CA65856).

References

1. Valk PE, Bailey DL, Townsend DW, Maisey MN, editors. Positron Emission Tomography: Basic Science and Clinical Practice. Part IV: Oncology. London: Springer, 2003:481–688.
2. Warburg O. On the origin of cancer cells. Science 1956;123:306–314.
3. Townsend DW, Cherry SR. Combining anatomy with function: the path to true image fusion. Eur Radiol 2001;11:1968–1974.
4. Beyer T, Townsend DW, Brun T, Kinahan PE, Charron M, Roddy R, et al. A combined PET/CT scanner for clinical oncology. J Nucl Med 2000;41:1369–1379.
5. Charron M, Beyer T, Bohnen NN, Kinahan PE, Dachille M, Jerin J, Nutt R, et al. Image analysis in patients with cancer studied with a combined PET and CT scanner. Clin Nucl Med 2000; 25:905–910.
6. Meltzer CC, Martinelli MA, Beyer T, Kinahan PE, Charron M, McCook B, et al. Whole-body FDG PET imaging in the abdomen: value of combined PET/CT. J Nucl Med 2001;42:35P.
7. Meltzer CC, Snyderman CH, Fukui MB, Bascom DA, Chander S, Johnson JT, et al. Combined FDG PET/CT imaging in head and neck cancer: impact on patient management. J Nucl Med 2001;42:36P.
8. Kluetz PG, Meltzer CC, Villemagne VL, Kinahan PE, Chander S, Martinelli MA, et al. Combined PET/CT imaging in oncology: impact on patient management. Clin Positron Imaging 2000;3:223–230.
9. Hawkes DJ, Hill DL, Hallpike L, Bailey DL. Coregistration of structural and functional images. In: Valk P, Bailey DL, Townsend DW, Maisey MN, editors. Positron Emission Tomography: Basic Science and Clinical Practice. London: Springer, 2003:181–197.
10. Bailey DL, Meikle SR. A convolution-subtraction scatter-correction method for 3D PET. Phys Med Biol 1994;39:411–424.
11. Watson CC, Newport D, Casey ME. A single scatter simulation technique for scatter correction in 3D PET. In: Grangeat P, Amans J-L, editors. Three-Dimensional Image Reconstruction in Radiology and Nuclear Medicine. Dordrecht: Kluwer Academic, 1996:255–268.
12. Ollinger JM. Model-based scatter correction for fully 3D PET. Phys Med Biol 1996;41:153–176.
13. Casey ME, Nutt R. A multicrystal, two-dimensional BGO detector system for positron emission tomography. IEEE Trans Nucl Sci 1986;33:460–463.
14. Cho ZH, Farukhi MR. Bismuth germanate as a potential scintillation detector in positron cameras. J Nucl Med 1977;8:840–844.
15. Karp JS, Muehllehner G, Geagan MJ, Freifelder R. Whole-body PET scanner using curved-plate NaI(Tl) detectors. J Nucl Med 1998;39:50P.
16. Wienhard K, Eriksson L, Grootoonk S Casey M, Pietrzyk U, Heiss WD. Performance evaluation of the positron scanner ECAT EXACT. J Comput Assist Tomogr 1992;16:804–813.
17. Takagi K, Fukazawa T. Cerium-activated Gd_2SiO_5 single crystal scintillator. App Phys Lett 1983;42:43–45.
18. Melcher CL, Schweitzer JS. Cerium-doped lutetium oxyorthosilicate: a fast, efficient new scintillator. IEEE Trans Nucl Sci 1992;39:502–505.

19. Townsend DW, Isoardi RA, Bendriem B. Volume imaging tomographs. In: Bendriem B, Townsend DW, editors. The Theory and Practice of 3D PET. Dordrecht: Kluwer, 1998:111–132.
20. Spinks TJ, Jones T, Bailey DL, Townsend DW, Grootoonk S, Bloomfield PM. Physical performance of a positron tomograph for brain imaging with retractable septa. Phys Med Biol 1992;37:1637–1655.
21. Strother SC, Casey ME, Hoffman EJ. Measuring PET scanner sensitivity: relating count rates in the image to signal-to-noise ratios using noise equivalent counts. IEEE Trans Nucl Sci 1990;37:783–788.
22. Kinahan PE, Rogers JG. Analytic three-dimensional image reconstruction using all detected events. IEEE Trans Nucl Sci 1990;36:964–968.
23. Defrise M, Kinahan PE, Townsend DW, Michel C, Sibomana M, Newport DF. Exact and approximate rebinning algorithms for 3D PET data. IEEE Trans Med Imaging 1997;16:145–158.
24. Hudson H, Larkin R. Accelerated image reconstruction using ordered subsets of projection data. IEEE Trans Med Imaging 1994;13:601––609.
25. Comtat C, Kinahan PE, Defrise M, Michel C, Townsend DW. Fast reconstruction of 3D PET data with accurate statistical modeling. IEEE Trans Nucl Sci 1998;45:1083–1089.
26. Daube-Witherspoon ME, Matej S, Karp JS, Lewitt RM. Application of the row action maximum likelihood algorithm with spherical basis functions to clinical PET imaging. IEEE Trans Nucl Sci 2001;48:24–30.
27. Watson CC. New, faster image-based scatter correction for 3D PET. In: IEEE Nuclear Science Symposium and Medical Imaging Conference, Toronto, Canada, November 1999, pp 1637–1641.
28. Townsend DW. A combined PET/CT scanner: the choices. J Nucl Med 2001;3:533-534.
29. Pelizzari CA, Chen GT, Spelbring DR, Weichselbaum RR, Chen CT. Accurate three-dimensional registration of CT, PET, and/or MR images of the brain. J Comput Assist Tomogr 1989;13:20–26.
30. Pietrzyk U, Herholz K, Heiss WD. Three-dimensional alignment of functional and morphological tomograms. J Comput Assist Tomogr 1990;14:51–59.
31. Woods RP, Mazziotta JC, Cherry SR. MRI-PET registration with automated algorithm. J Comput Assist Tomogr 1993;17:536–546.
32. Townsend DW, Beyer T, Blodgett TM. PET/CT scanners: a hardware approach to image fusion. Semin Nucl Med 2003;XXXIII(3):193–204.
33. Kinahan PE, Townsend DW, Beyer T, Sashin D. Attenuation correction for a combined 3D PET/CT scanner. Med Phys 1998;25:2046–2053.
34. Burger C, Goerres G, Schoenes S, Buck A, Lonn AH, von Schulthess GK. PET attenuation coefficients from CT images: experimental evaluation of the transformation of CT into PET 511-keV attenuation coefficients. Eur J Nucl Med Mol Imaging 2002;29:922–927.
35. Rappoport V, Carney J, Townsend DW. X-Ray tube voltage dependent attenuation correction scheme for PET/CT scanners. IEEE MIC Abstract Book 2004;M10-76:213.
36. Yau YY, Chan WS, Tam YM, Vernon P, Wong S, Coel M, et al. Application of intravenous contrast in PET/CT: does it really introduce significant attenuation correction error. J Nucl Med 2005;46:283–291.
37. Carney JP, Townsend DW. CT-based attenuation correction for PET/CT scanners. In: von Schultess G, editor. CLINICAL PET, PET/CT and SPECT/CT: Combined Anatomic-Molecular Imaging. Baltimore: Lippincott, Williams & Wilkins, 2003:46–58.
38. Antoch G, Freudenberg LS, Egelhof T, et al. Focal tracer uptake; a potential artifact in contrast-enhanced dual-modality PET/CT scans. J Nucl Med 2002;43:1339–1342.
39. Antoch G, Freudenberg LS, Beyer T, Bockisch A, Debutin JF. To enhance or not to enhance? ^{18}F-FDG and CT contrast agents in dual-modality ^{18}F-FDG PET/CT. J Nucl Med 2004;45(suppl):56S–65S.
40. Goerres GW, Hany TF, Kamel E, Von Schulthess GK, Buck A. Head and neck imaging with PET and PET/CT: artifacts from dental metallic implants. Eur J Nucl Med 2002;29:367–370.
41. Kamel EM, Burger C, Buck A, Von Schulthess G, Goerres G. Impact of metallic dental implants on CT based-AC in a combined PET/CT scanner. Eur Radiol 2003;13:724–728.
42. Goerres GW, Burger C, Kamel E, et al. Respiration-induced attenuation artifact at PET/CT; technical considerations. Radiology 2003;226:906–910.
43. Townsend DW, Yap JT, Carney JPJ, Long M, Hall NC, Bruckbauer T, et al. Respiratory gating with a 16-slice LSO PET/CT scanner. J Nucl Med 2004;45(5):165P (abstract).
44. Beyer T, Antoch G, Muller S, et al. Acquisition protocol considerations for combined PET/CT imaging. J Nucl Med 2004;45(suppl):25S–35S.
45. Halpern B, Dahlbom M, Quon A, et al. Impact of patient weight and emission scan duration on PET/CT image quality and lesion detectability. J Nucl Med 2004;45:797–801.
46. Coleman RE, Delbeke D, Guiberteau MJ, Conti PS, Royal HD, Weinreb JC, et al. Intersociety Dialogue on Concurrent PET/CT with an Integrated Imaging System. From the Joint ACR/SNM/SCBT-MR PET/CT Working Group. J Nucl Med 2005;46:1225–1239.